

AD-A111 853

AEROSPACE CORP EL SEGUNDO CA SPACE SCIENCES LAB

F/G 20/9

ELECTRIC FIELDS AND PLASMA WAVES RESULTING FROM A BARIUM INJECT--ETC(U)

JAN 82 H C KOONS, M B PONGRATZ

F04701-81-C-0082

UNCLASSIFIED

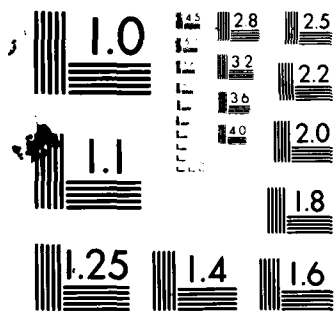
TR-0082(2940-06)-1

SD-TR-81-112

NL

1-1
A1
A1-1

END
DATE
FILMED
4 82
DTIC



MICROCOPY RESOLUTION TEST CHART
NATIONAL BUREAU OF STANDARDS-1963-A

ADA111853

Electric Fields and Plasma Waves Resulting from a Barium Injection Experiment

H. C. KOONS
Space Sciences Laboratory
The Aerospace Corporation
El Segundo, Calif. 90245

and

MORRIS B. PONGRATZ
University of California
Los Alamos Scientific Laboratory
Los Alamos, N. Mex. 87545

18 January 1982

APPROVED FOR PUBLIC RELEASE;
DISTRIBUTION UNLIMITED

Prepared for
SPACE DIVISION
AIR FORCE SYSTEMS COMMAND
Los Angeles Air Force Station
P.O. Box 92960, Worldway Postal Center
Los Angeles, Calif. 90009

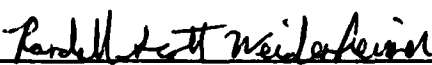
DTIC
ELECTE
MAR 10 1982
A


DTIC FILE COPY

This report was submitted by The Aerospace Corporation, El Segundo, CA 90245, under Contract No. F04701-81-C-0082 with the Space Division, Deputy for Technology, P.O. Box 92960, Worldway Postal Center, Los Angeles, CA 90009. It was reviewed and approved for The Aerospace Corporation by G. A. Paulikas, Director, Space Sciences Laboratory. Lieutenant R. S. Weidenheimer, SD/YLVS was the project officer for the Mission-Oriented Investigation and Experimentation (MOIE) Program.


This report has been reviewed by the Public Affairs Office (PAS) and is releasable to the National Technical Information Service (NTIS). At NTIS, it will be available to the general public, including foreign nations.

This technical report has been reviewed and is approved for publication. Publication of this report does not constitute Air Force approval of the report's findings or conclusions. It is published only for the exchange and stimulation of ideas.


Randall S. Weidenheimer, 2nd Lt, USAF
Project Officer


Florian P. Meinhardt, Lt Col, USAF
Director, Advanced Space
Development

FOR THE COMMANDER


Norman W. Lee, Jr., Col, USAF
Deputy for Technology

UNCLASSIFIED

SECURITY CLASSIFICATION OF THIS PAGE (When Data Entered)

REPORT DOCUMENTATION PAGE		READ INSTRUCTIONS BEFORE COMPLETING FORM
1. REPORT NUMBER SD-TR-81-112	2. GOVT ACCESSION NO.	3. RECIPIENT'S CATALOG NUMBER
4. TITLE (and Subtitle) ELECTRIC FIELDS AND PLASMA WAVES RESULTING FROM A BARIUM INJECTION EXPERIMENT		5. TYPE OF REPORT & PERIOD COVERED
		6. PERFORMING ORG. REPORT NUMBER TR-0082(2940-06)-1
7. AUTHOR(s) Harry C. Koons and Morris B. Pongratz		8. CONTRACT OR GRANT NUMBER(s) F04701-81-C-0082
9. PERFORMING ORGANIZATION NAME AND ADDRESS The Aerospace Corporation El Segundo, Calif. 90245		10. PROGRAM ELEMENT, PROJECT, TASK AREA & WORK UNIT NUMBERS
11. CONTROLLING OFFICE NAME AND ADDRESS Space Division Air Force Systems Command Los Angeles, Calif. 90009		12. REPORT DATE 18 January 1982
14. MONITORING AGENCY NAME & ADDRESS (if different from Controlling Office)		13. NUMBER OF PAGES 43
		15. SECURITY CLASS. (of this report) Unclassified
16. DISTRIBUTION STATEMENT (of this Report) Approved for public release; distribution unlimited.		
17. DISTRIBUTION STATEMENT (of the abstract entered in Block 20, if different from Report)		
18. SUPPLEMENTARY NOTES		
19. KEY WORDS (Continue on reverse side if necessary and identify by block number) Barium Release Ion-Cyclotron Waves Plasma Emissions Rocket Experiment		
20. ABSTRACT (Continue on reverse side if necessary and identify by block number) A shaped-charge, barium plasma injection experiment was performed in June 1976 from the DOE Kauai Test Facility. The rocket payload contained seven shaped charges - a sevenfold larger package than the typical payloads employed in previous barium plasma injections conducted in this program. An attitude-control system oriented the injection perpendicular to the local geomagnetic field. The injection altitude was 450 km. The second-stage motor section contained a payload to measure dc and ac electric fields using		

DD FORM 1473
(FACSIMILE)

UNCLASSIFIED

SECURITY CLASSIFICATION OF THIS PAGE (When Data Entered)

UNCLASSIFIED

SECURITY CLASSIFICATION OF THIS PAGE(When Data Entered)

19. KEY WORDS (Continued)

20. ABSTRACT (Continued)

a 5-m-long, tip-to-tip dual spherical probe antenna. The ac electric field frequency response was from 100 Hz to 12 kHz. The dc channel responds up to 160 Hz. Shortly after the detonation the dc electric field was parallel to the geomagnetic field. A few seconds later the measured electric field was the $\vec{v} \times \vec{B}$ field induced by the motion of the antenna through the plasma. A variety of plasma waves were detected for approximately 20 s following the injection. The initial impulse in the dc channel was measured to be 115 mV/m. The injection generated barium cyclotron waves at 3.4, 7.2, and 10.6 Hz. The barium gyrofrequency at the altitude of the injection was 3.3 Hz. The initial amplitude at 3.4 Hz was 25 mV/m peak-to-peak. These waves were evident in the data for approximately 6 s. Between 3 and 8 s after the explosion, band-limited noise was intermittently present between 1.6 and 3.2 kHz. These emissions were lower-hybrid-resonance emissions in a barium plasma. The instability responsible for these emissions is tentatively identified as the modified two stream instability. Wide-band noise with a decreasing intensity as a function of frequency in the band from 100 Hz to 5 kHz was present from 4 to 30 seconds following the explosion. The intensity maximized when the antenna was most nearly parallel to the geomagnetic field. This suggests that the waves were ion acoustic waves. Highly structured emissions occurred between 500 Hz and 2.5 kHz for several seconds beginning 17 s after the explosion. The wave mode responsible for these structured emissions has not yet been identified.

UNCLASSIFIED

SECURITY CLASSIFICATION OF THIS PAGE(When Data Entered)

SUMMARY

A variety of interesting plasma wave phenomena was observed during a barium injection experiment. Ion cyclotron waves and lower-hybrid-resonance emissions were positively identified in the data. Alfvén waves and an oblique shock wave in the ambient plasma and ion acoustic waves in the barium plasma are tentatively identified in the data. Detailed measurements of the ion and electron densities and velocity space distributions with high time resolution are required to properly identify the instabilities involved. With such instrumentation, plasma-injection experiments will become a valuable technique for studying the complex interactions occurring in large scale plasmas.

ACCESSION NO.
DTIC NUMBER
DTIC CLASS
DTIC ABSTRACT
DTIC INDEX



A

PREFACE

We are grateful to B. Whalen for the ion density data; to D. C. Pridmore-Brown for the power spectrum calculations, and to H. Hilton and P. Daly for the attitude determination. We are also grateful to Bob Jeffries, the Buaro project leader, at the Los Alamos Scientific Laboratories and to Al Hutters, Herman Winte, John Moyer and Win Watson of Sandia Laboratories, Albuquerque, and W. B. Harbridge and C. W. Jordan of The Aerospace Corporation for their efforts in assembling and launching the rocket and payloads.

This work was supported by the U. S. Air Force under Contract F04701-79-C-0080, LASL under DOE Contract W-740S-ENG-36, and Sandia under DOE contract AT(29-1)789.

CONTENTS

SUMMARY	1
PREFACE	3
I. INTRODUCTION	11
II. DESCRIPTION OF PAYLOADS	17
dc and ac Field Experiments	17
Thermal Ion Detector	22
Energetic Electron Detectors	23
Attitude Determination	24
III. EVENT MORPHOLOGY	27
Prompt Features in the ULF Spectrum	30
dc Fields	33
Contact Potential	38
IV. PLASMA WAVES	43
Ion Cyclotron Waves	43
Lower-Hybrid-Resonance Emissions	45
Ion-Acoustic Waves	46
Whistler-Mode Waves	48
Unidentified Emissions	48
REFERENCES	49

FIGURES

1.	Geometry of the explosive shaped charge	18
2.	Relative logarithmically spaced contours of equal initial barium atom velocity space density for an injection perpendicular to the geomagnetic field	19
3.	Geometry of the barium injection (top) and the antenna system (bottom)	25
4.	Photograph of the neutral barium at $E + 15$ s in 553.5-nm light	28
5.	Photograph of the ionized barium at $E + 27$ s in 455.4-nm light	29
6.	A record of the dc field measurement (top). The remainder of the figure shows the direction cosines of the antenna axis \vec{A} with respect to vector directions derived from the rocket-velocity vector \vec{V} and the geometric field vector \vec{B}	31
7.	Temporal variation of the ion density measured by the Thermal Ion Detector (top). Spectrogram of event-related ac electric fields (bottom)	32
8.	Geometry of the neutral atom (Ba) and ion + flow in the plane defined by the geomagnetic field vector B and the rocket velocity vector V	34
9.	Power spectral density of the ultra-low-frequency electric- field data for the three-second interval preceding the shaped-charge detonation	36
10.	Power spectral density of the ultra-low-frequency electric- field data for the three-second interval from 3 to 6 s following the barium injection	37
11.	A record of the dc field measurement from 4 to 17 s following the barium injection (top). The direction cosine of the antenna axis \vec{A} with respect to the geo- magnetic field vector \vec{B} (middle). The direction cosine of the antenna axis with respect to the motionally induced electric field direction $\vec{V} \times \vec{B}$ (bottom)	39

FIGURES (Continued)

12.	Offset of the measured dc potential from the predetonation level as a function of time after the barium injection	40
13.	Power spectral density of the ultra-low-frequency electric field data for the three-second interval from 0 to 3 s following the barium injection	44
14.	An intensified photograph of the Buaro injection taken at Event + 1.5 s through an interference filter designed to pass the 630.0-nm line of (¹ D)	47

TABLES

1.	Plasma Parameters at Event Plus 1 s, 10 km from the Injection Point	13
2.	Summary of Plasma Instability Criteria	15
3.	Measurements Performed by the dc Experiment	21

I. INTRODUCTION

Barium plasma injection experiments in the ionosphere allow one to study a variety of plasma instabilities that may occur in large scale plasmas. Plasma microinstabilities are generally considered to be responsible for the transfer of energy from an energetic plasma to a cooler plasma in situations where the binary collision mean free path is much longer than the observed coupling scale size. Examples of anomalous, collisionless coupling occur in high altitude nuclear explosions and at the bow shock interface between the solar wind and the magnetosphere. In the latter, the shock thickness measured by satellites is much smaller than the classical, binary collision mean free path in the solar wind. A variety of plasma waves resulting from the detonation of small barium canisters in the ionosphere were detected by Kelley et al. [1974]. The highest frequency waves displayed a sharp low-frequency cutoff near the lower-hybrid-resonance frequency.

A plasma injection experiment also provides an opportunity to examine mechanisms that produce striations or plasma density fluctuations in ionospheric plasmas [Schutz et al., 1973]. Because the total number of emitters (barium ions) in a striation remains relatively constant with time, barium ion plasmas are ideally suited for long-term studies of striation parameters.

Buaro (the Spanish word for buzzard) is the code name selected for the shaped-charge, barium plasma injection experiment launched on June 7, 1976 from the DOE Kauai Test Facility (22.06° N, 200.21° E). The experiment was designed to investigate plasma instabilities and striation phenomena first observed in a similar experiment, code named Loxia, conducted May 14, 1975 [Pongratz, 1975]. The Buaro rocket payload contained seven shaped charges -- a sevenfold larger package than the typical payloads employed in the thirteen previous barium plasma injections conducted in this program since October 1971 [Wescott et al., 1974, 1975a, b; Pongratz, 1975]. An attitude control system aligned

the injection perpendicular to the geomagnetic field. Onboard diagnostic instrument packages provided in situ measurements of the electric and magnetic fields and energy distributions of charged particles. Ground stations located at the DOE observatories atop Mt. Haleakala on Maui and near the launch site on Kauai photographed optical emissions.

Because of the new payload design, the technical objectives were both scientific and engineering in nature as follows: 1) To investigate the wave-particle plasma interactions resulting from injection of a dense barium plasma perpendicular to the geomagnetic field, 2) To investigate electron heating and the subsequent ambient excitations resulting from such an injection, 3) To investigate plasma striation mechanisms concurrently in both collisional and collisionless environments, and 4) To evaluate the engineering design and performance of the sevenfold larger shaped-charge payload.

Lampe et al. [1975] reviewed several plasma microinstabilities that may result from high-altitude shaped-charge barium plasma injections perpendicular to the magnetic field. The barium injection may also be subject to Harris-type anisotropic velocity space instabilities [Krall and Trivelpiece, 1973; Simons et al., 1979] not considered by Lampe et al., [1975], but important in controlled fusion applications. In general, the instabilities amplify electrostatic or electromagnetic waves that produce coupling between the fast barium ions and the ambient ionospheric ions or barium photoelectrons through wave-particle interactions.

We now briefly examine the beam-plasma microinstabilities that may have been excited in the Buaro experiment. Table 1 lists some of the Buaro plasma parameters 1 s after the detonation, 10 km from the event point in the direction of the shaped-charge injection. The parameters are based on a model for the injected barium plasma. Maui ionosonde data were used to construct electron density vs. height profiles. The Maui ionosonde is about 4 deg east of the barium injection location. The height of the

Table 1. Plasma parameters at Event Plus 1 s, 10 km from the Injection Point.
The subscript i refers to barium ions and the subscript j refers to atomic oxygen ions.

ION DRIFT VELOCITY, U	$U_i = 1 \times 10^6 \text{ cm/s}$	$U_j = 0$
ION TEMPERATURE, T	$T_i = 4.1 \text{ eV}$	$T_j = 3.17 \text{ eV}$
ION THERMAL SPEED, V	$V_i = 1.7 \times 10^5 \text{ cm/s}$	$V_j = 1.0 \times 10^5 \text{ cm/s}$
ELECTRON TEMPERATURE AND THERMAL SPEED	$T_e = 3.0 \text{ eV}$	$V_e = 7.3 \times 10^7 \text{ cm/s}$
ION SOUND SPEED	$C_i = 1.4 \times 10^5 \text{ cm/s}$	$C_j = 7.3 \times 10^4 \text{ cm/s}$
DENSITIES	$n_i = 1 \times 10^6 \text{ cm}^{-3}$	$n_e = 1 \times 10^6 \text{ cm}^{-3}$
MAGNETIC FIELD	$B = 0.30 \text{ Gauss}$	
ELECTRON CYCLOTRON AND PLASMA FREQUENCIES	$f_{be} = 840 \text{ kHz}$	$f_{pe} = 9.1 \text{ MHz}$
ION CYCLOTRON FREQUENCIES	$f_{bi} = 3.3 \text{ Hz}$	$f_{bj} = 28.6 \text{ Hz}$
ION MASS	$m_i = 137 \text{ amu}$	$m_j = 16 \text{ amu}$
ION PLASMA FREQUENCIES	$f_{pi} = 17.5 \text{ kHz}$	$f_{pj} = 9.1 \text{ kHz}$
LOWER HYBRID FREQUENCIES	$f_{Hi} = 1.6 \text{ kHz}$	$f_{Hj} = 5.3 \text{ kHz}$
LARMOR RADIUS	$\rho_i = 4.8 \times 10^4 \text{ cm}$	$\rho_e = 1.4 \times 10^1 \text{ cm}$
ELECTRON DEBYE LENGTH	$\lambda_D = 1.3 \text{ cm}$	
LENGTH OF MACROSCOPIC SYSTEM PARALLEL TO B	$L = 2 \times 10^5 \text{ cm}$	
ELECTRON PLASMA BETA	$\beta_e = 1.3 \times 10^{-3}$	

maximum electron density in the F-layer of the ionosphere at 0430 UT was 350 km. The topside profiles are estimated from the curvature of the electron-density profile near the altitude of maximum electron density. The ambient electron density at the injection altitude just prior to the injection is $3 \times 10^4 \text{ cm}^{-3}$.

The Buaro plasma parameters listed in Table 1 can be used to determine whether or not this plasma satisfies the instability conditions given by Lampe et al. [1975]. Conditions for five possible instabilities are examined. In general, the free energy for the instabilities is contained in the velocity of the barium ions in the beam, not by gradients in the beam. The types of instabilities are distinguished by the modes of the waves they amplify. The five instabilities are 1) magnetized ion-ion, 2) unmagnetized ion-ion, 3) modified two-stream, 4) ion acoustic, and 5) beam cyclotron. Each instability requires that electromagnetic stabilization is absent and the wavelength parallel to B be small compared to the system size L. The latter condition generally is not met in electron or ion-gun type injections. Table 2 gives the results of comparing the plasma described in Table 1 with the instability conditions.

TABLE 2. Summary of Plasma Instability Criteria

<u>Instability</u>	<u>Unstable</u>	<u>Effective Collision Frequency</u>	<u>Comments</u>
Magnetized ion-ion	Yes	$\sim 1 \times 10^3 \text{ s}^{-1}$	
Unmagnetized ion-ion	No	—	Stabilized by electron shielding
Modified two-stream	Yes	$\sim 6 \times 10^8 \text{ s}^{-1}$	
Ion acoustic	No	—	Photoelectrons too cold
Beam cyclotron	Yes		

The beam-cyclotron instability could rapidly heat electrons, making the plasma then subject to the otherwise precluded ion-acoustic instability.

Diagnostic instrumentation on the Buaro rocket was designed to study the manifestations of the plasma instabilities expected.

II. DESCRIPTION OF PAYLOADS

The Buaro launch vehicle, a Strypi 4R sounding rocket, carried a double payload. The second-stage motor section contained electric and magnetic field sensors, plasma and energetic-particle detectors, and a sun sensor. The separable forward payload section contained high-explosive shaped charge and conical barium-liner assemblies. Separated at launch plus 110 s, the two payloads were about 1.2 km apart at the time that the shaped charge was exploded. The forward section also contained a gyro-controlled attitude control system (ACS) developed by Sandia Laboratories. The ACS used four gas bottles to despin the payload to 1 rps and to orient the shaped charges to the proper injection angle. In the Buaro experiment, the ACS oriented the injection perpendicular to both the local geomagnetic field and to a vector from the Maui observation station to the event point.

The seven shaped charges were held in a light foam matrix and arranged in a cluster as shown in Fig. 1. Each cone contained 1450 g of barium. Assuming that about 30 percent of the barium metal was shock vaporized, approximately 1.3×10^{25} atoms of barium were released. Of this, about one-half of the barium atoms would be in the directed jet of fast atoms; the remainder is essentially thermalized and expands with a Gaussian shape at ~ 1.7 km/s. The center-of-mass of this portion of the distribution moves along the rocket trajectory at ~ 0.7 km/s. Figure 2 shows the expected neutral barium velocity distribution in the rocket frame of reference. The contours are equal velocity space density.

dc and ac Field Experiments. The second-stage motor section contained a payload provided by The Aerospace Corporation to measure dc and ac electric fields using a dual spherical probe antenna. The antenna was 5-m-long tip-to-tip and was deployed perpendicular to the longitudinal axis of the rocket section. The ac electric-field

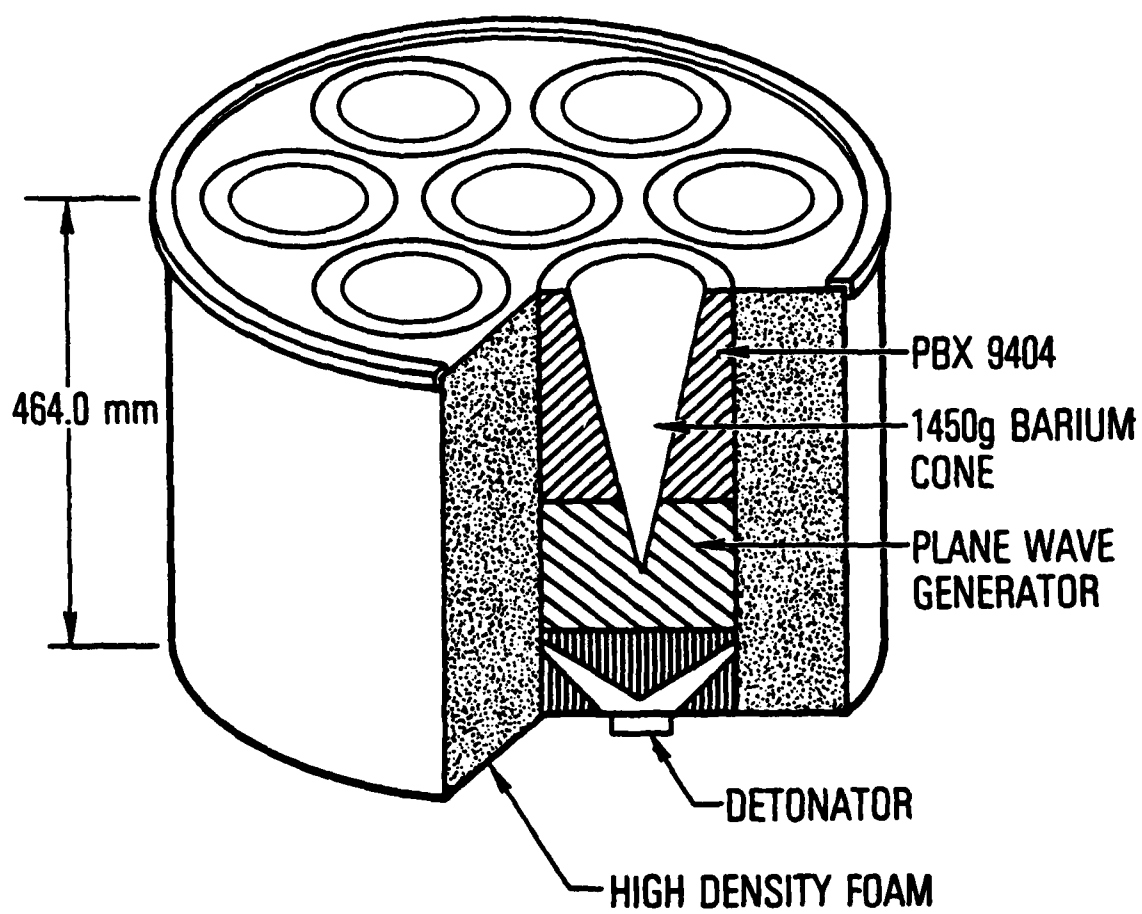


Fig. 1. Geometry of the explosive shaped charge

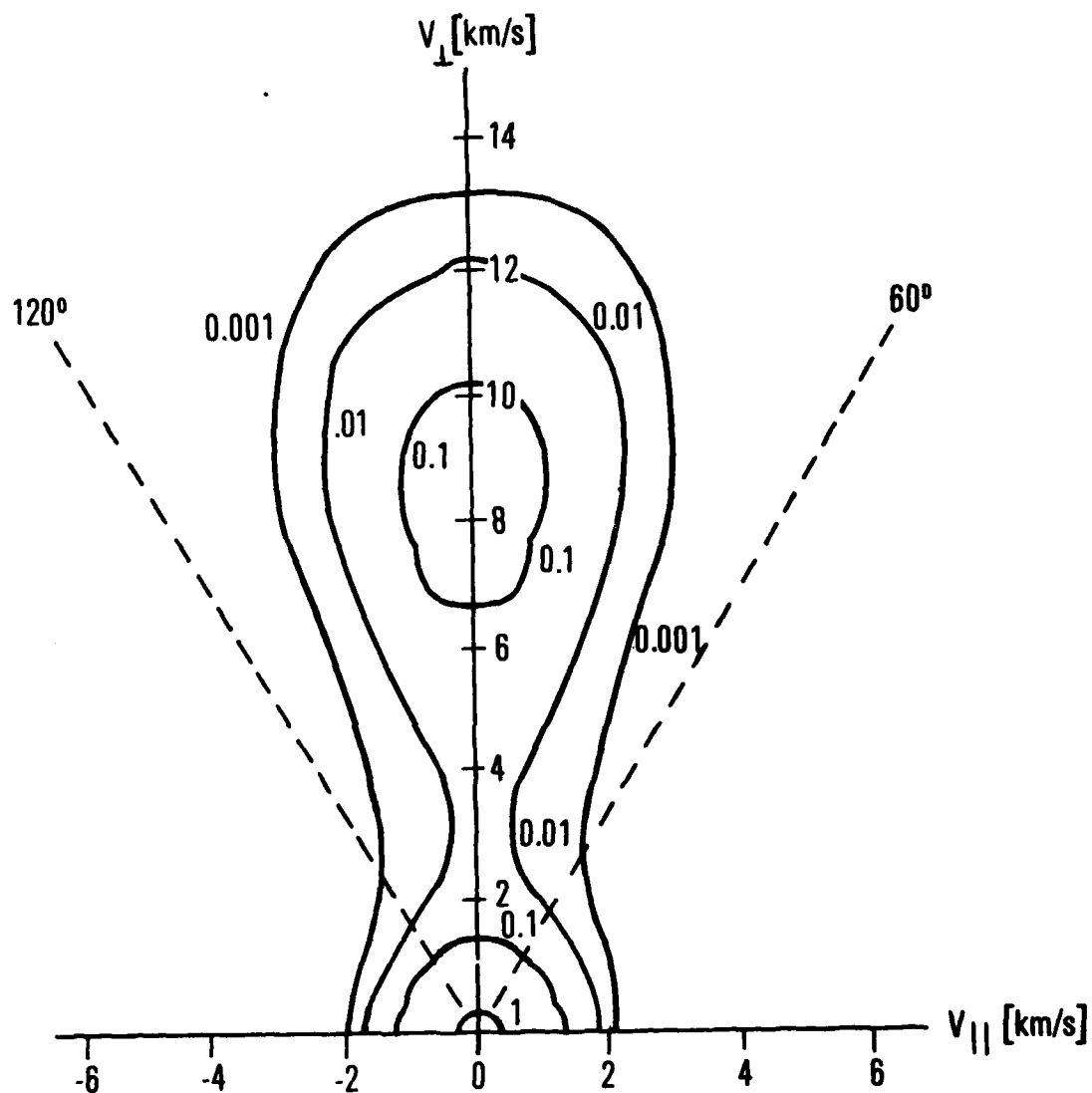


Fig. 2. Relative logarithmically spaced contours of equal initial barium atom velocity space density for an injection perpendicular to the geomagnetic field

experiment had a frequency response from 100 Hz to 12 kHz. This analog signal was transmitted FM-FM on the baseband of a 248.6-MHz carrier. The dc experiment consisted of two measurements, each designed to perform in two modes as shown in Table 3. In the primary mode the potential difference between the two probes was monitored. Measurement No. 2 telemetered this potential difference directly in the range ± 200 mV. In the event that a large contact potential was present, Measurement No. 1 contained an integration circuit with a 10-s integration time to remove the dc bias and keep the measurement on scale. Measurement No. 1 telemetered the potential difference in the range ± 400 mV.

In the secondary mode of operation, one probe was grounded to the rocket frame (the reference for the differential measurement) and the potential difference between a single probe and the vehicle was measured for 1 out of 10 s. In this mode, Measurement No. 1 was telemetered in the range ± 800 mV and Measurement No. 2 in the range ± 400 mV.

From the dc-experiment data, it is apparent that several anomalies occurred in the instrumentation during the flight. All are attributed to high temperatures in the preamplifier enclosures, which were mounted close to the rocket motor in the lower section. The anomalies include phase shifts, which are unexplained, and mode switching failures. The mode switching capability was provided by a relay and driver circuit located in the preamplifier enclosure. The circuit was designed to operate at temperatures below 140°F . Above this temperature, the relay requires more current to switch states than the driver circuit can supply. Monitors indicated that the temperature in the preamplifier enclosure exceeded 220°F . Mode-switching failures occurred above 154°F . This temperature was reached at approximately 14:28:16: UT or ~240 seconds after launch.

Table 3. Measurements Performed by the dc Experiment

Measurement	Design	Range	Actual	Range
No. 1 - Primary Mode	$A_1 \cos \omega t + A_2 \cos \omega t + A_c$	$\pm 400 \text{ mV}$	$A_2 \cos(\omega t - 80^\circ) + A_c$	$\pm 400 \text{ mV}$
No. 1 - Secondary Mode	$A_2 \cos \omega t$	± 800	Failed	
No. 2 - Primary Mode	$A_1 \cos \omega t + A_2 \cos \omega t$	± 200	$A_1 \cos(\omega t + 80^\circ) + A_2 \cos(\omega t - 80^\circ)$ $= 2 A_1 \cos \omega t \cos 80^\circ$	± 200
No. 2 - Secondary Mode	$A_2 \cos \omega t$	± 400	$A_2 \cos(\omega t - 80^\circ)$	± 200

A_1 and A_2 are the magnitudes of the potentials between probes one and two and the vehicle respectively.
 A_c is the contact potential. The phase is measured with respect to the predicted phase of the 1.1 Hz spin modulation on the motionally induced field.

The actual behavior of the dc experiment during flight was determined by comparing the phase and amplitude from the two measurements with those predicted for the motionally induced field component ($\vec{v} \times \vec{B} \cdot \vec{A}$) along the antenna at 0433 UT. The result is shown in Table 3. The behavior was checked using the calculated amplitude of $\vec{v} \times \vec{B} \cdot \vec{A}$ and the functional forms in Table 3 to compute the amplitude and phase of the two measurements at 0429 UT. At that time the amplitude was about half that at 0433 UT; the phase of $\vec{v} \times \vec{B} \cdot \vec{A}$ was significantly different, since rocket apogee occurred between these times. The agreement at 0429 UT was quite good, satisfying us that the behavior was understood and that it was the same before and after the barium injection.

Measurement No. 2 went into its secondary mode 1.75 s after the barium detonation. The signal change that occurred at that time precluded its use for spectral analysis. The spectral analyses results described below were obtained from Measurement No. 1. Measurement No. 2 was used as the phase reference when it was in its primary mode.

Thermal Ion Detector. The Canadian National Research Council (NRC) provided instruments to detect energetic electrons and thermal ions. The Thermal Ion Detector (TID) section of this package measured positive ions with energies from 0 to 5 eV using electrostatic analysis and channeltron detectors. There are two TID units in the NRC package: one oriented at 45° and one at 90° to the longitudinal axis. Observations were telemetered in an FM-FM-PCM format, using a 93.0 kHz VCO on a 239.4 MHz transmitter. The TID obtains a 40-point ion-energy spectrum every 200 ms with energy resolution of about five percent. The energy geometric factor is approximately $10^{-6} \text{ cm}^2\text{-sr-eV}$.

Energetic Electron Detectors. The NRC package contained an electrostatic analyzer to measure electrons with energies from 100 eV to 20 keV in 16 channels, with energy resolution of about 10 percent. The electrons are detected with channeltrons, with a complete energy spectrum obtained every 3.2 s. The energy geometric factor is about $5 \times 10^{-4} \text{ cm}^2\text{-sr-eV}$.

The NRC package also contained a solid state detector to measure electrons with energies greater than about 20 keV or protons with energies above about 25 keV. The electron spectrum is measured every 5 ms in three integral channels with energies beginning at 25, 50, and 100 keV. The detector geometric factor is about $10^{-2} \text{ cm}^2\text{-sr}$.

The Aerospace Corporation provided a high-energy electron detector on the second stage. Five logarithmically spaced differential energy channels between 100 keV and 1 MeV and an integral channel for electron energies above 1 MeV were sampled every 25 ms. Electrons are detected with a 400-mm^2 surface-barrier detector with a geometric factor of $\sim 0.5 - 1.0 \text{ cm}^2\text{-sr}$. The count-rate meter signals were commutated and telemetered FM-FM on 70.0 kHz VCO on the 239.4-MHz transmitter. The detector is oriented 70° from the longitudinal axis of the rocket section.

Preliminary examination of the data indicates that the electron telescope turned on and was functioning. The three lowest energy channels were counting, immediately after turn on, at a rate of 10 to 20 counts per second. Speculation is that the surface-barrier detector had warmed up sufficiently to stimulate the lower thresholds. This is somewhat substantiated by the gradual decay of the outputs toward zero during the flight. No particles attributable to the barium injection were detected.

Attitude Determination. Magnetometers and a solar sensor instrumented by Sandia Laboratories were used to determine the orientation of the spinning second stage. The magnetometers measure the magnetic field along (longitudinal) and perpendicular (radial) to the longitudinal axis of the vehicle, with a resolution of about five percent of the geomagnetic field intensity.

A spring-release mechanism consisting of three springs equally spaced about the circumference of the rocket was designed to separate the upper section containing the barium from the lower section containing the diagnostic instruments. Following release, the motor section was expected to remain spinning with its angular momentum vector parallel to the vehicle axis. However, the spring forces were apparently unequal and the lower section began to tumble. Almost three minutes after release, a new equilibrium orientation was established with the angular momentum vector perpendicular to the vehicle axis, as shown in Fig. 3. This orientation was verified using the magnetometer and sun sensor data at 0429 UT and 0433 UT, i.e., one minute before and three minutes after the event. The error in the aspect angles is estimated to be 2 deg. In this anomalous orientation the sun crossed the sun sensor along a diagonal, rather than perpendicular to its V-shaped slits. This produced the major contribution to the error.

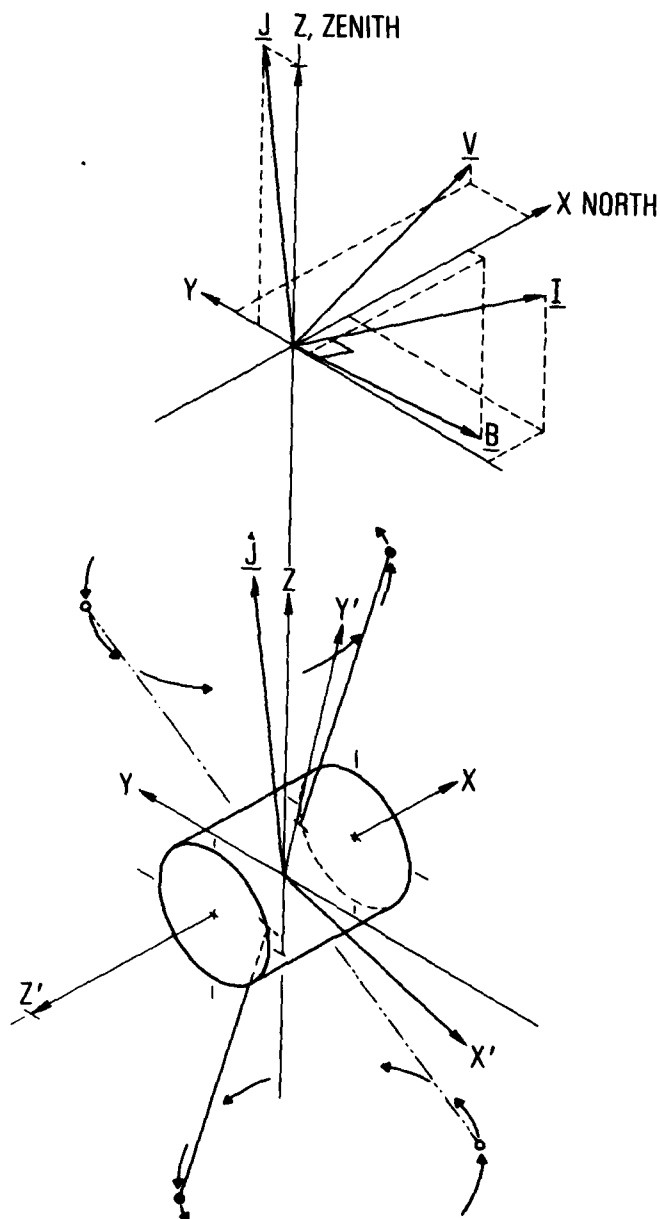


Fig. 3. Geometry of the barium injection (top) and the antenna system (bottom). (X, Y, Z) is a geographic coordinate system and (X', Y', Z') is the rocket reference coordinate system. \vec{J} is the rocket angular momentum vector, \vec{V} is the rocket velocity vector, \vec{B} is the geomagnetic field vector and \vec{I} is the barium injection direction perpendicular to \vec{B} . The rocket section and antennas are shown to scale.

III. EVENT MORPHOLOGY

The shaped-charge assembly was timer-detonated at 14:30:01.266 UT (E), June 7, 1976, at an altitude of 450 km less than 1 s before rocket apogee.

The event was initially well centered in the cameras that provided the real time tracking of the debris cloud. The fast neutral barium jet was clearly visible to the TV instrumentation at both stations in the shape of an elongated tear drop. It was also visible to the naked eye. A highly structured debris cloud remained in the event area. A field-aligned streak extended from the detonation location by $E + 25$ s and was striated in less than 1 min, as observed from both Maui and Kauai. The Maui and Kauai stations used Image Orthicons pointed near the zenith to observe the fast ions passing overhead along the geomagnetic field line through the event point. These ions were clearly discernible across the entire field of view from Maui by $E + 165$ s. By $E + 5$ min, striations appeared in the overhead streak that were very similar in spatial separation to the striations observed in the debris cloud. The ion streak was observed for about 20 min after the event. The debris cloud was tracked for about 35 min, although no dramatic changes were observed after about $E + 4$ min.

Figure 4 is a photograph taken from Maui at $E + 15$ s in 553.5-nm light. It records the neutral barium distribution from which the velocity distribution can be estimated. Figure 5 is a photograph taken from Maui at $E + 27$ s in 455.4-nm light. It records the orientation and distribution of the barium ion jet and it shows the field alignment of the ions and striations forming on the backside of the debris cloud.

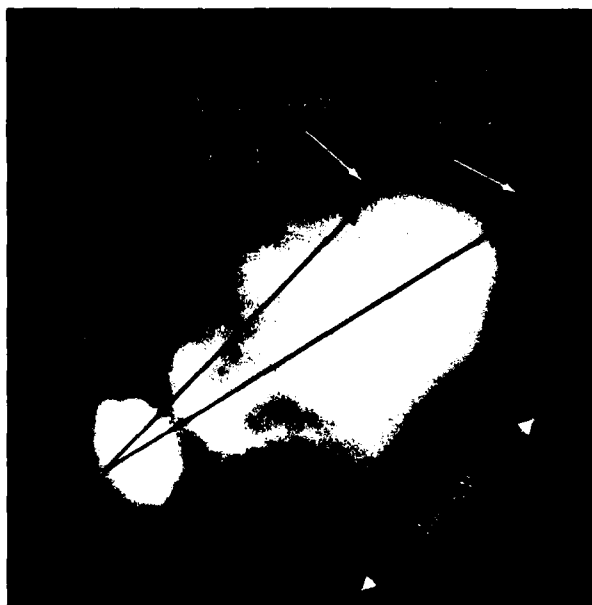


Fig. 4. Photograph of the neutral barium at $E + 15$ s in 553.5-nm light. The photograph taken from Maui shows the distribution of neutral barium in the plan defined by a vector \vec{I} in the direction of the injection and B .



Fig. 5. Photograph of the ionized barium at $E + 27$ s in 455, 4-nm light. The photograph taken from Maui shows the field alignment of the ions and striations forming on the backside of the cloud.

Prompt Features in the ULF Spectrum. At essentially the instant of the detonation, the dc probe data in Figure 6 show a negative excursion. This is most likely the prompt arrival of an Alfvén wave. The Alfvén speed in the background O^+ plasma is ~ 950 km/s. The travel time of such a fast wave would not be resolved by the instrumentation. The amplitude of this wave was not sufficient to register in the magnetometer data, which had a resolution of 8 mG.

At approximately 0.2 s after the detonation, a large positive signal is observed in the probe data. The amplitude in the dc channel was 115 mV/m. Assuming that the detonation occurred 1.2 km ahead of the detector as planned, the speed of the phenomenon responsible for this feature is ~ 6 km/s. Although this is about one-half the speed of the energetic barium injected perpendicular to the geomagnetic field, it is unlikely that any of these ions have reached the detector on this time scale. The geometry is such that the cyclotron motion of the ions moves them away from the direction of the second section of the rocket and the neutrals in the jet do not strike the second stage of the rocket. The first ions to reach the rocket would be those in the thermal distribution, which is expanding at ~ 1.7 km/s.

It is possible that this feature is propagated as a slow wave in the background plasma. The ion sound speed in a $2000^\circ K$ O^+ plasma is 2 km/s. If the ratio of the propagation speed to the sound speed is identified as a Mach number, the speed is Mach 3, suggesting a shock propagating at an oblique angle to the magnetic field. However, the thermal ion detector measured no plasma enhancement associated with the passage of this feature. The ion density data are shown in Figure 7. Immediately after the detonation, there was an abrupt decrease in the O^+ plasma density followed by a gradual recovery. This was due to charge-exchange dissociative-recombination chemistry and has been described by Pongratz et al. [1977].

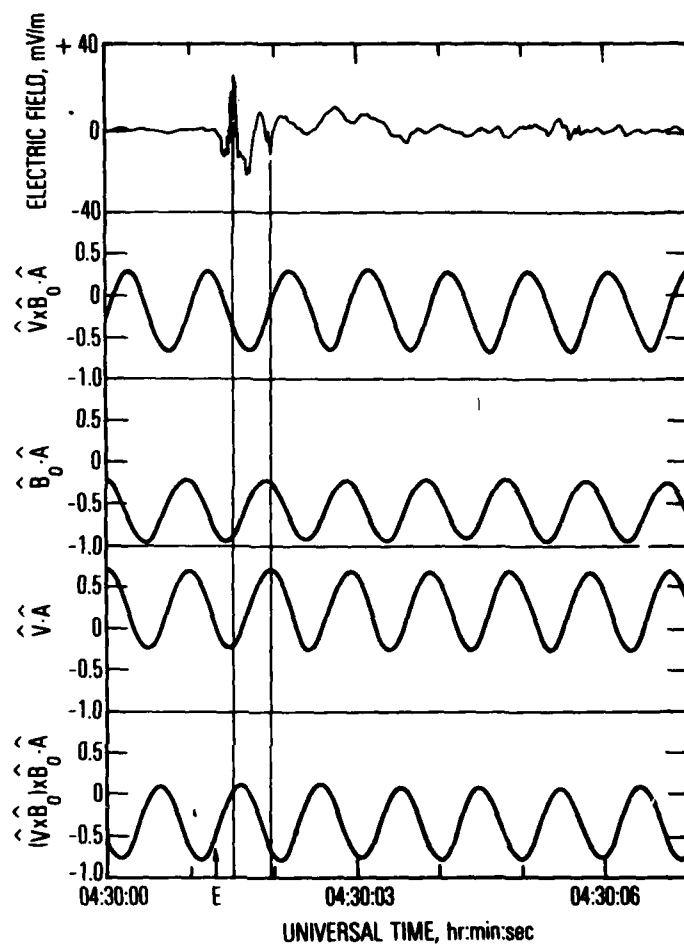


Fig. 6. A record of the dc field measurement (top). The remainder of the figure shows the direction cosines of the antenna axis \hat{A} with respect to vector directions derived from the rocket-velocity vector \hat{V} and the geometric field vector \hat{B} . See Fig. 8 for a diagram showing the reference directions. The time of the detonation is denoted by E.

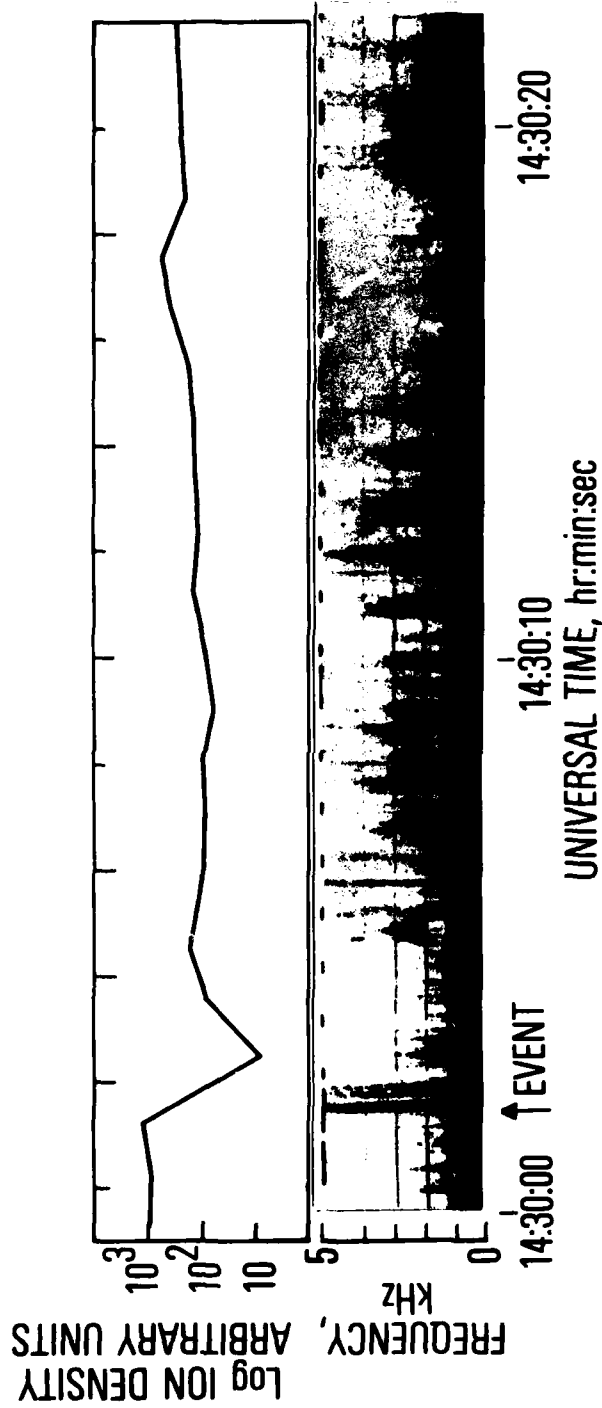


Fig. 7. Temporal variation of the ion density measured by the Thermal Ion Detector (top). Spectrogram of event-related ac electric fields (bottom). A wide band impulse is detected at the time of the explosion. Between 3 and 8 s after the explosion, band limited noise is intermittently present between 1.6 and 3.2 kHz. The lower band edge is the barium lower-hybrid-resonance frequency.

The negative excursion of the dc measurement at 0.65 s after the detonation corresponds with a travel velocity of 1.85 km/s. The velocity of the thermal barium was expected to be about 1.7 km/s. We identify this feature with the arrival of the thermal barium at the second section of the rocket. The thermal ion detector data are not resolved to this accuracy. By 1.2 s after the detonation, the O^+ density was depleted by approximately two orders of magnitude.

The next phenomenon observed in the dc data after the arrival of the barium is the ion cyclotron waves described below.

dc Fields. Following the detonation, four directions are conceivable for the dc electric field at the diagnostic section of the rocket. These directions are identified in Fig. 8. This figure is drawn in the symmetry plane that contains the velocity and geomagnetic-field vectors. Prior to the detonation, the electric field is motionally induced in the direction $\vec{v} \times \vec{B}$. If A is the instantaneous direction of the antenna axis, the field component measured is $\vec{v} \times \vec{B} \cdot \vec{A}$.

Following the detonation the following possibilities might occur:

Case 1. Since the second section of the rocket trails the first by about 1.2 km along the same trajectory, the detonation is in the direction of the velocity vector as shown in Fig. 8. If the ions are streaming radially away from the detonation, the polarization field would be in the same direction as the motionally included field prior to the detonation and the $\vec{v} \times \vec{B} \cdot \vec{A}$ component would be enhanced.

Case 2. However, the ions are inhibited from crossing the magnetic field and, as shown in Fig. 8, the ion distribution is thoroughly field aligned. Imagine a neutral barium atom, denoted by the symbol Ba in Fig. 8, streaming radially away from the detonation

DETONATION

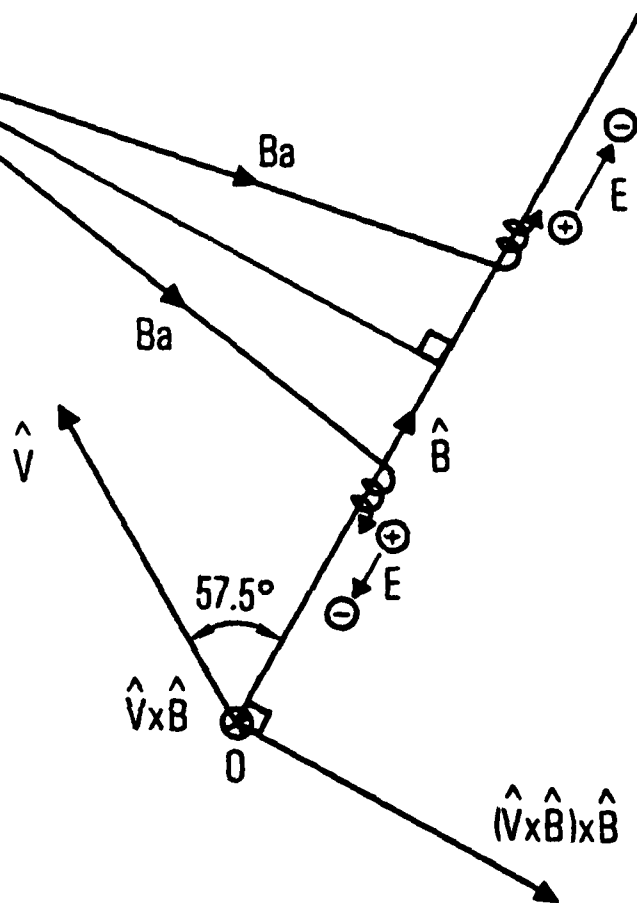


Fig. 8. Geometry of the neutral atom (Ba) and ion + flow in the plane defined by the geomagnetic field vector B and the rocket velocity vector V . Ions arriving at the rocket shortly after the detonation were ionized on the flux tube passing through the rocket. The various directions shown correspond with the reference directions for the antenna direction cosines plotted in Fig. 6.

point and becoming photoionized. The ion then moves parallel to \vec{B} . The faster electrons move ahead of the ions, producing a diffusion electric field antiparallel to \vec{B} at the location of the second section of the rocket as shown in Fig. 8.

Case 3. It is conceivable that there could be an electric field directed radially away from the detonation. This would be the case if the plasma pressure from the detonation exceeded the magnetic pressure. This is not expected to be the case in the Buaro Experiment.

Case 4. If a radial field is generated but is quickly shorted parallel to \vec{B} , the resulting component would be perpendicular to B in the symmetry plane, i.e., in the direction $(\vec{v} \times \vec{B}) \times \vec{B}$.

Figure 6 contains the dot product of the unit vector corresponding to each of the above four cases with the unit vector \vec{A} pointing in the direction of the antenna axis. Since the rocket section is rotating at approximately 1 rps about the angular momentum axis shown in Fig. 3, the measured component oscillates at ~ 1 Hz. The instantaneous value of each component can be read from Fig. 6.

A large 1-Hz component should be present in the power spectrum if a significant dc field is present in any of the four directions identified above. The power spectrum obtained just prior to the detonation is shown in Fig. 9. The largest peak at the low-frequency end is at 1 Hz and corresponds to the motionally induced field component of 13.3 mv/m peak-to-peak along the antenna. The power spectrum for the time period from 3 to 6 s after the detonation is shown in Fig. 10. The power in the 1-Hz component has been reduced by a factor of ~ 4 .

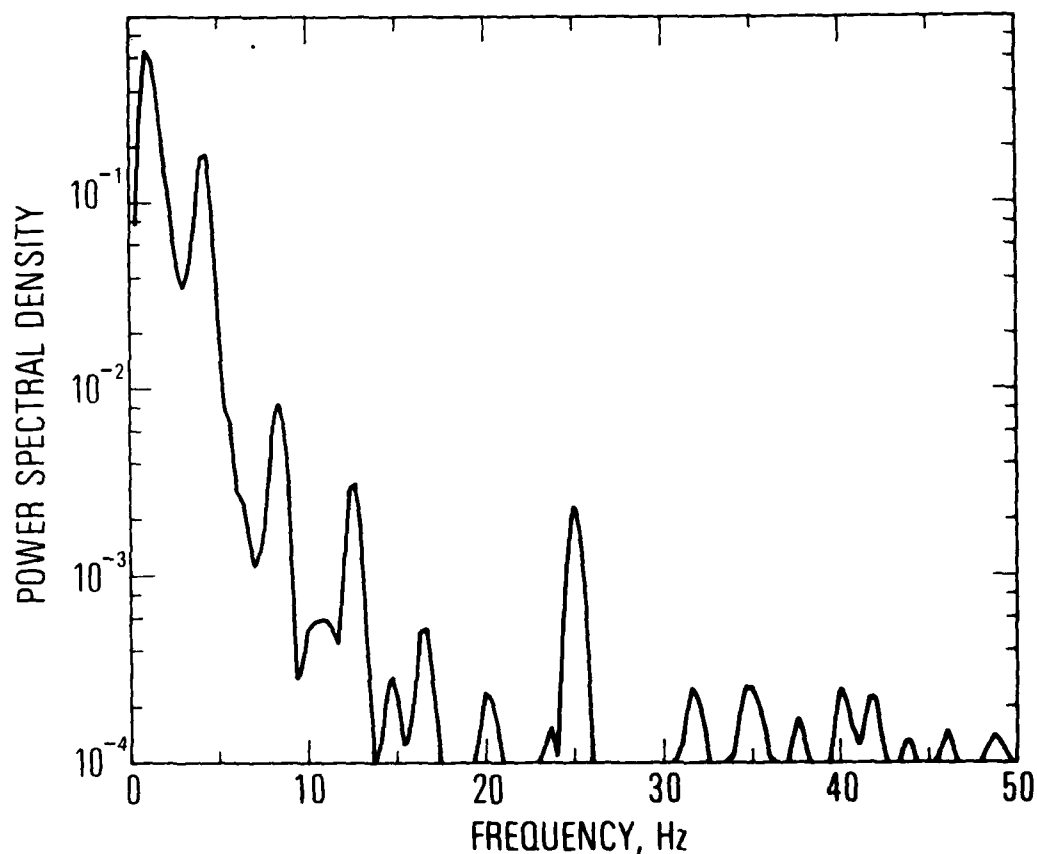


Fig. 9. Power spectral density of the ultra-low-frequency electric-field data for the three-second interval preceding the shaped-charge detonation. The largest amplitude peak at 1.0 Hz corresponds with the spin rate (1.1 Hz) of the vehicle. The remaining peaks at 4.33, 8.33, 12.67, 20.00 and 25.00 Hz are harmonically related. The fundamental frequency is 4.17 Hz. This is the fourth harmonic of the rocket spin frequency.

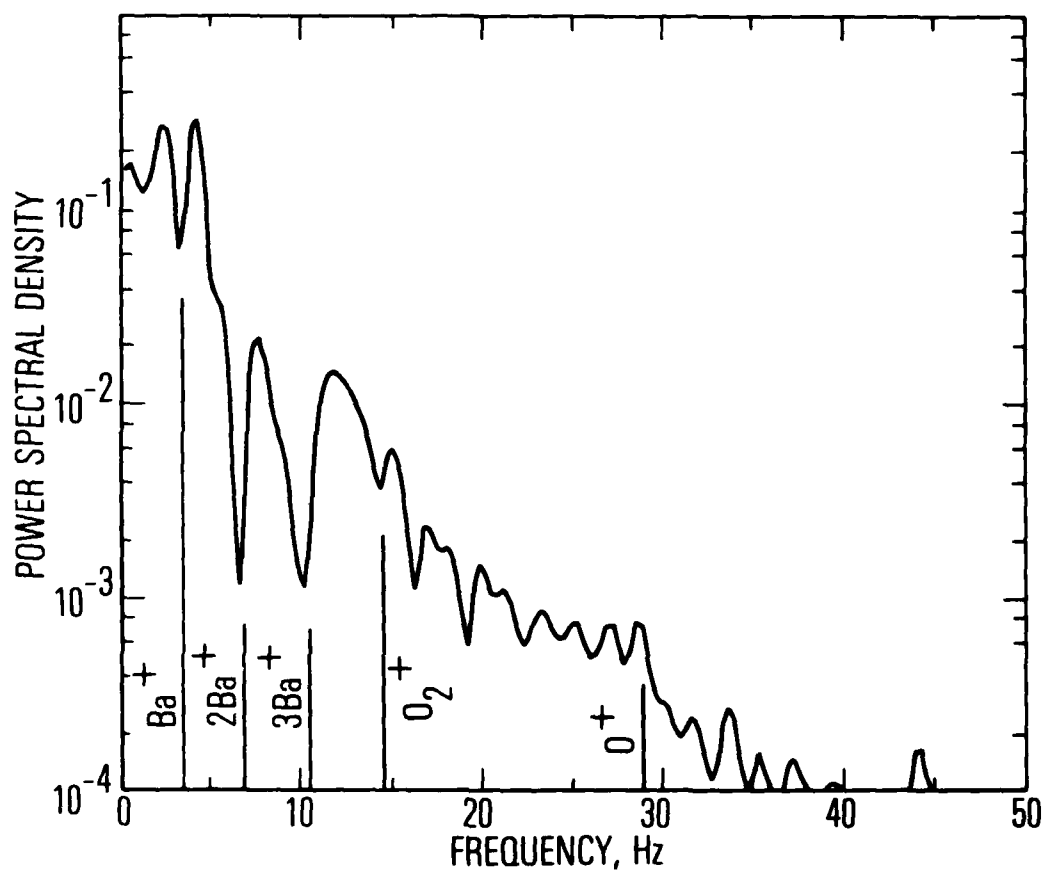


Fig. 10. Power spectral density of the ultra-low-frequency electric-field data for the three-second interval from 3 to 6 s following the barium injection. Ion gyrofrequencies and the harmonics of the barium ion gyrofrequency are identified by vertical lines.

At later times, the 1-Hz component is again apparent in the dc data (Fig. 11). Between 6 and 16 s after the detonation, the direction of the field rotates. From 6 to 10 s, the measured field is in phase with $\vec{B} \cdot \vec{A}$. This implies that, for a short time after the detonation, the dc electric field had a significant component parallel to the geomagnetic field at the payload. By 15 s after the detonation, the measured field is in phase with $\vec{v} \times \vec{B} \cdot \vec{A}$ and the amplitude has returned to that expected for the motionally induced field. The direction of the dc field is thus not observed to be in the direction required for gradient instabilities [Mikhailovskii, 1974].

Contact Potential. The dc potential in Measurement No. 1 reached a maximum excursion of 320 mV from its predetonation level at 0.35 s after the injection. Its subsequent behavior is plotted in Fig. 12. The potential decayed exponentially with a time constant of 0.66 s. Superimposed upon this decay is the 3.3-Hz Ba^+ cyclotron wave. Following this initial rapid decay, smaller variations persisted for 4 s. Finally, the potential decayed from 100 mV to its predetonation value with a time constant of 5.8 s. Superimposed upon this gradual decay is a modulation at the 1.1-Hz spin frequency. If this potential is attributed to an electric field component in the plasma, the field would be 40 mV/m 6 s after the detonation. The direction of the field must be such that the component along the rotating antenna system is essentially constant. None of the computed components shown in Fig. 6 show a large offset with a small modulation.

Only a very small amount of the thermal barium will coat the spherical probe. Assuming that one-half of the barium is in the spherically expanding distribution and that all of the barium that strikes a probe remains on the surface the coating will be $\sim 10^{13}$ atoms/cm². Since a typical surface has $O(10^{15})$ atoms/cm², roughly one percent of the surface is contaminated by Ba and somewhat more by H₂O from the

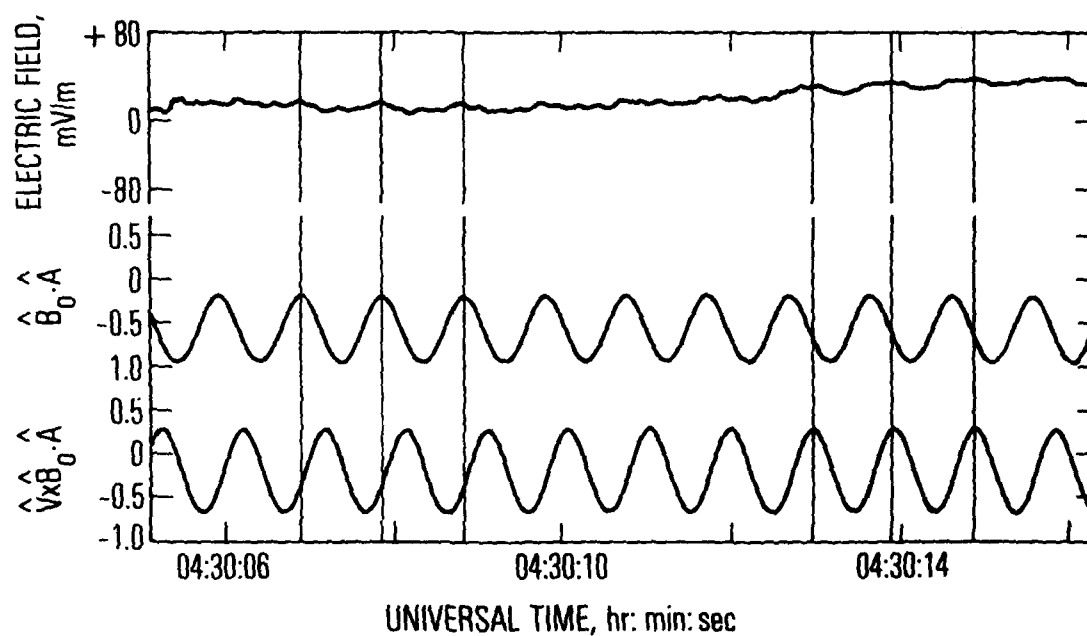


Fig. 11. A record of the dc field measurement from 4 to 17 s following the barium injection (top). The direction cosine of the antenna axis \hat{A} with respect to the geomagnetic field vector \hat{B} (middle). The direction cosine of the antenna axis with respect to the motionally induced electric field direction $\hat{V} \times \hat{B}$ (bottom).

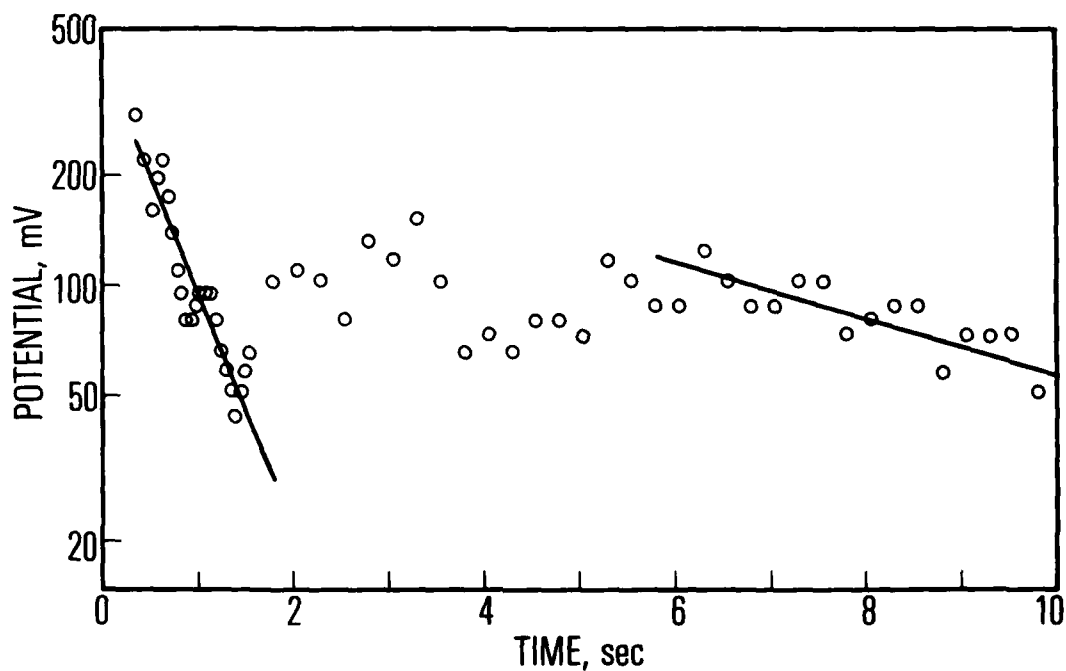


Fig. 12. Offset of the measured dc potential from the predetonation level as a function of time after the barium injection

explosion products. The work function difference between a carbon (Aquadag) and a barium surface is ~ 1.8 V. The amount of contamination expected in this experiment should cause less than 10 percent of the observed potential change.

The potential change may be due to a change in the electrical parameters of the circuit. Both the capacitance and resistance of the plasma sheaths surrounding the probes and the second stage will change as the density, temperature, and effective ionic mass change [Koons et al., 1970]. The time scale of the observed potential change is comparable to that of the low mass ions. The plasma diagnostic measurements are not sufficient to quantitatively verify this hypothesis.

IV. PLASMA WAVES

Ion Cyclotron Waves. A variety of plasma waves were detected for approximately 20 s following the detonation. In this section, we describe only those detected below the oxygen gyrofrequency. The analog record from the dc channel is shown at the top of Figure 6. The time of the detonation is identified by the arrow labeled E.

The analog data (Fig. 6) were digitized at a sample rate of 500 samples per second and spectrum analyzed in three-second intervals using a fast fourier-transform technique employing a Hanning lag window [Jenkins and Watts, 1968]. The power spectral density is calculated at 0.33-Hz intervals and the effective bandwidth is 1.11 Hz. The spectrum during the three-second interval immediately following the detonation is shown in Fig. 13. The dominant peak at the low frequency end occurs at 3.33 Hz and corresponds with the barium gyrofrequency which is 3.34 Hz in the 0.3-G geomagnetic field at the detonation altitude. Emission lines of Ba^+ , O_2^+ , Al^+ , OH^+ , and O^+ are identified in the spectrum.

The intervals comprising the time from 2 to 7 s after the detonation are characterized by a broadband spectrum extending from below the barium gyrofrequency at 3.3 Hz to just above the oxygen gyrofrequency at 28.6 Hz. The most notable feature of these spectra is stopbands at the barium gyrofrequency and its first and second harmonics, as shown in Fig. 10.

A more complete description and interpretation of the ion cyclotron wave data from this experiment is given by Koons and Pongratz [1978]. Simons et al. [1979] have numerically solved the dispersion relation for electrostatic instabilities of the drift-loss-cone type for a velocity distribution appropriate to the Buaro experiment. They find a low-frequency wave that they interpret to be the source of prompt striations observed in Buaro, and drift cyclotron loss-cone instabilities that correspond to the ion cyclotron waves described above.

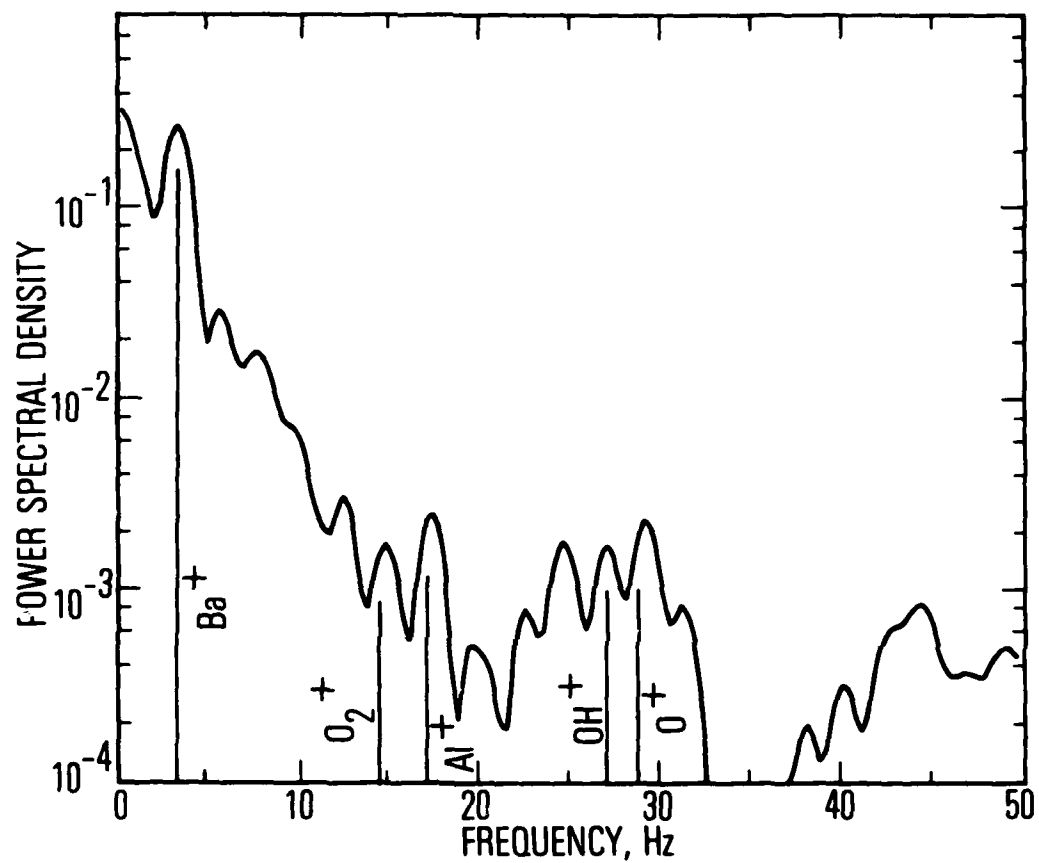


Fig. 13. Power spectral density of the ultra-low-frequency electric field data for the three-second interval from 0 to 3 s following the barium injection. Ion gyrofrequencies are identified by vertical lines.

Lower-Hybrid-Resonance Emissions. The extremely-low-frequency wave spectrum and amplitude are shown in Fig. 7. Approximately 200 ms after the detonation, a wideband impulse of 2 mV/m rms was detected. A large number of smaller impulses appearing in the record before and after the barium injection are attributed to sferics penetrating the ionosphere.

Between 3 and 10 s after the event, an irregular noise band appears between 1.5 and 4 kHz. Returning to the plasma parameters in Table 1, the band is readily identified with the barium lower-hybrid-resonance frequency.

Lampe et al. [1975] have reviewed and summarized several plasma microinstabilities that may be applicable to high-altitude shaped-charge barium plasma injections, perpendicular to the magnetic field. The electrostatic dispersion relation for the modified two-stream instability when electrons and one species of ions, in this case Ba^+ , have a relative drift across the magnetic field is [Lampe et al., 1975]

$$1 - \frac{\omega_{LHR}^2 \Theta^2}{\omega^2} - \frac{\omega_{LHR}^2}{(\omega - k U_{ie})^2} = 0$$

where $\Theta = \theta (\omega_{pe}/\omega_{pi})$ is the effective mass angle, θ the propagation direction with respect to the geomagnetic field, and U_{ie} is the relative electron-ion drift velocity.

For the model plasma parameters at E + 1 s, 10 km from the explosion, the largest angle for hydrodynamic instability occurs for $\Theta = 2$.

The wave phase velocity

$$v_{ph} = U_{ie} \left(1 - \frac{1}{2} \Theta^{-2/3}\right) + U_e$$

for $U_{ie} = 10^4$ m/s and $U_e = 0$ is 6.9×10^3 m/s.

The wavelength of maximum growth is

$$\lambda = 2\pi/k = 2\pi U_{ie}/\sqrt{3} \omega_{LHR} = 0.3m .$$

The frequency of maximum growth is

$$\omega = \omega_{LHR} (1 - \frac{1}{2} \Theta^{-2/3}) = 1.4 \omega_{LHR}$$

and the growth rate is

$$\gamma = 2^{-4/3} \sqrt{3} \Theta^{1/3} \omega_{LHR} = 0.87 \omega_{LHR} .$$

The waves observed in a band above the barium lower-hybrid-resonance frequency were most likely the result of a modified two-stream instability of the type described by Lampe et al. [1975].

Ion-acoustic Waves. Beginning at approximately 14:30:09 UT, wide-band emissions from ~ 100 Hz to ~ 5 kHz appear in the ac spectrum (see Fig. 7). These signals are modulated at the spin rate. The maxima occur when the antenna axis is parallel to the geomagnetic field. The signals show no absorption lines or banded structure that would be expected for cyclotron waves. They are tentatively identified as ion acoustic waves with their wave normals essentially parallel to the geomagnetic field.

The observation of ion-acoustic waves would suggest a high T_e/T_i ratio. Further evidence for the existence of hot electrons is shown in Fig. 14, which is a photograph of the Buaro event at $E + 1.5$ s. The camera that recorded the picture used electrostatic image intensification, and an interference filter designed to pass the 630.0-nm line of

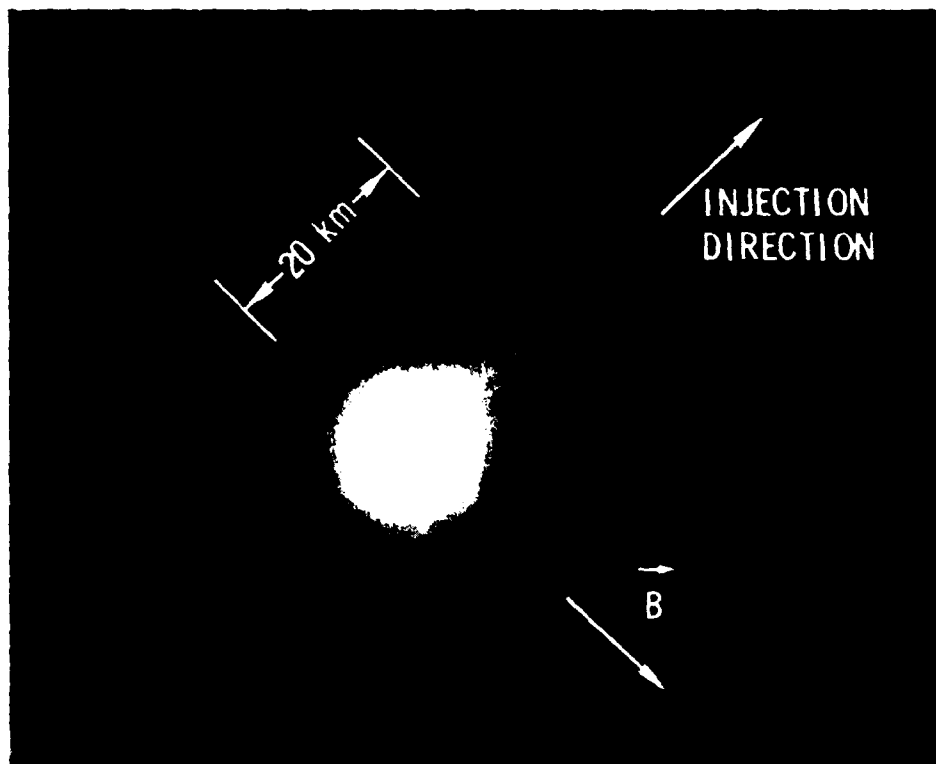


Fig. 14. An intensified photograph of the Buaro injection taken at Event + 1.5 s through an interference filter designed to pass the 630.0-nm line of (1D). The directions of the shaped-charge injection and of the geomagnetic field are identified on the figure.

O(1D) was placed in front of the objective lens. Note the narrow pointed emission feature going up and to the right in Fig. 14. This feature is located in the very center of the fast barium beam. We believe that this was caused by electronic excitation of OI from the ground state to the 1D level and then subsequent radiative transition at 630.0 nm back to the ground state. This hypothesis would indicate that electrons were heated to energies in excess of 2 eV by the injection process. A variety of plasma instabilities, including the modified two-stream [Lampe et al., 1975; Simons and Pongratz, 1977] and the drift-cyclotron [Simons et al., 1979] could be responsible for the electron heating. Huba and Ossakow [1979] have suggested that collisional effects in inhomogeneous plasmas could destroy cyclotron resonances, demagnetize ions and electrons, and lead to the growth of lower hybrid and ion-acoustic waves. Bohmer and Fornaca [1978] observe electron heating under similar conditions in laboratory plasmas.

Whistler-Mode Waves. The signal between 4 and 5 kHz just prior to 14:30:12 UT is a whistler generated by a lightning stroke in the atmosphere. Several such whistlers were detected during the flight; however, no whistler-mode waves that might have been generated by the barium injection were observed.

Unidentified Emissions. The structured emissions at 14:30:20 UT have not been identified. The fundamental frequency and spacing of the lines is very nearly equal to the proton gyrofrequency; however, protons are not likely to be present at this altitude.

REFERENCES

- Böhmer, H. and S. Fornaca, Experiments on nonlinear effects of strong ion cyclotron wave turbulence, UIC Tech. Rpt. No. 78-84, Univ. Calif., Irvine, Calif., 1978.
- Huba, J. D., and S. L. Ossakow, Destruction of cyclotron resonances in weakly collisional, inhomogeneous plasmas, NRL Memorandum Rpt. 3916, Naval Research Laboratory, Washington, D. C., April, 1979.
- Jenkins, G. M. and D. G. Watts, Spectral Analysis and its Applications, Holden Day, San Francisco, Ca., 1968.
- Kelley, M. C., A. Pedersen, U. V. Fahleson, D. Jones, and D. Köhn, Active experiments stimulating waves and particle precipitation with small ionospheric barium releases, J. Geophys. Res., **79**, 2859, 1974.
- Koons, H. C., D. A. McPherson, and W. B. Harbridge, Dependence of very-low-frequency electric field antenna impedance on magnetospheric plasma density, J. Geophys. Res., **75**, 2490, 1970.
- Krall, N. A., and A. W. Trivelpiece, Principles of Plasma Physics, McGraw Hill, New York, N. Y., p. 497, 1973.
- Lampe, M., W. M. Manheimer and K. Papadopoulos, Anomalous transport coefficients for HANE applications due to plasma micro-instabilities, NRL Memorandum Rpt. 3076, Naval Research Laboratory, Washington, D.C., 1975.
- Mikhailovskii, A. B., Theory of Plasma Instabilities, Vol. 2. Instabilities of an Inhomogeneous Plasma, Consultants Bureau, New York, N. Y., 1974.
- Pongratz, M. B., Wave-particle pitch angle diffusion produced by injecting barium plasma perpendicular to the geomagnetic field, Trans. Am. Geophys. Un., **56**, 1052, 1975.
- Pongratz, M. B., G. M. Smith, C. D. Sutherland, J. Zinn, P. Daly, B. A. Whalen, and T. E. Eastman, Artificial holes in the F region ionosphere: theory and experiment, Trans. Am. Geophys. Un., **58**, 455, 1977.
- Schutz, S., G. J. Adams, and F. S. Mozer, Probe electric field measurements near a midlatitude ionospheric barium release, J. Geophys. Res., **78**, 6634, 1973.

Simons, D. J., and M. B. Pongratz, "Micro-Instabilities Active in Perpendicular Shaped Charge Injections," EOS, 58, transactions, American Geophysical Union, 1977.

Simons, D. J., M. B. Pongratz and S. Peter Gary, Prompt strations in ionospheric barium clouds due to a velocity space instability J. Geophys. Res., accepted for publication, 1979.

Wescott, E. M., E. P. Rieger, H. C. Stenbaek-Nielsen, T. N. Davis, H. M. Peek, and P. J. Bottoms, L=1.24 conjugate magnetic field line tracing experiments with barium shaped charges, J. Geophys. Res., 79, 159, 1974.

Wescott, E. M., H. C. Stenbaek-Nielsen, T. N. Davis, W. B. Murcray, H. M. Peek, and P. J. Bottoms, The L=6.6 Oosik barium plasma injection experiment and magnetic storm of March 7, 1972, J. Geophys. Res., 80, 951, 1975a.

Wescott, E. M., E. P. Rieger, H. C. Stenbaek-Nielsen, T. N. Davis, H. M. Peek, P. J. Bottoms, The L=6.7 quiet time barium shaped charge injection experiment 'Chachalaca', J. Geophys. Res., 80, 2738, 1975b.

LABORATORY OPERATIONS

The Laboratory Operations of The Aerospace Corporation is conducting experimental and theoretical investigations necessary for the evaluation and application of scientific advances to new military space systems. Versatility and flexibility have been developed to a high degree by the laboratory personnel in dealing with the many problems encountered in the nation's rapidly developing space systems. Expertise in the latest scientific developments is vital to the accomplishment of tasks related to these problems. The laboratories that contribute to this research are:

Aerophysics Laboratory: Launch vehicle and reentry aerodynamics and heat transfer, propulsion chemistry and fluid mechanics, structural mechanics, flight dynamics; high-temperature thermomechanics, gas kinetics and radiation; research in environmental chemistry and contamination; cw and pulsed chemical laser development including chemical kinetics, spectroscopy, optical resonators and beam pointing, atmospheric propagation, laser effects and countermeasures.

Chemistry and Physics Laboratory: Atmospheric chemical reactions, atmospheric optics, light scattering, state-specific chemical reactions and radiation transport in rocket plumes, applied laser spectroscopy, laser chemistry, battery electrochemistry, space vacuum and radiation effects on materials, lubrication and surface phenomena, thermionic emission, photosensitive materials and detectors, atomic frequency standards, and bioenvironmental research and monitoring.

Electronics Research Laboratory: Microelectronics, GaAs low-noise and power devices, semiconductor lasers, electromagnetic and optical propagation phenomena, quantum electronics, laser communications, lidar, and electro-optics; communication sciences, applied electronics, semiconductor crystal and device physics, radiometric imaging; millimeter-wave and microwave technology.

Information Sciences Research Office: Program verification, program translation, performance-sensitive system design, distributed architectures for spaceborne computers, fault-tolerant computer systems, artificial intelligence, and microelectronics applications.

Materials Sciences Laboratory: Development of new materials: metal matrix composites, polymers, and new forms of carbon; component failure analysis and reliability; fracture mechanics and stress corrosion; evaluation of materials in space environment; materials performance in space transportation systems; analysis of systems vulnerability and survivability in enemy-induced environments.

Space Sciences Laboratory: Atmospheric and ionospheric physics, radiation from the atmosphere, density and composition of the upper atmosphere, aurorae and airglow; magnetospheric physics, cosmic rays, generation and propagation of plasma waves in the magnetosphere; solar physics, infrared astronomy; the effects of nuclear explosions, magnetic storms, and solar activity on the earth's atmosphere, ionosphere, and magnetosphere; the effects of optical, electromagnetic, and particulate radiations in space on space systems.

. . .

